



## Single-atom alloy with Pt-Co dual sites as an efficient electrocatalyst for oxygen reduction reaction

Xing Cheng<sup>a</sup>, Yueshuai Wang<sup>b</sup>, Yue Lu<sup>b</sup>, Lirong Zheng<sup>c</sup>, Shaorui Sun<sup>a</sup>, Hongyi Li<sup>b,\*</sup>, Ge Chen<sup>a,\*</sup>, Jiujun Zhang<sup>d,\*</sup>

<sup>a</sup> Beijing Key Laboratory for Green Catalysis and Separation, Faculty of Environment and Life, Beijing University of Technology, Beijing 100124, PR China

<sup>b</sup> Faculty of Materials and Manufacturing, Beijing University of Technology, Beijing 100124, PR China

<sup>c</sup> Beijing Synchrotron Radiation Facility, Institute of High Energy Physics, Chinese Academy of Sciences, Beijing 100049, PR China

<sup>d</sup> College of Sciences & Institute for Sustainable Energy, Shanghai University, Shanghai 200444, PR China



### ARTICLE INFO

#### Keywords:

Single-atom alloy  
Pt-Co dual sites  
Electrocatalyst  
Oxygen reduction reaction  
Operando XAS

### ABSTRACT

Reducing the usage of noble metals, such as platinum-based catalysts for oxygen reduction reaction (ORR) is pressingly demanded towards the practical applications of proton-exchange membrane fuel cells. One promising way is to develop Pt single atom catalysts (SACs), which, however, are plagued by their preference toward two-electron ORR pathway as well as stability issue. Herein, a single-atom alloy (SAA) catalyst with platinum-cobalt (Pt-Co) dual sites encapsulated in nitrogen-doped graphitized carbon nanotubes (Pt<sub>1</sub>Co<sub>100</sub>/N-GCNT) consisting of isolated Pt atoms decorated on the surface of Co nanoparticles was reported. Based on complementary spectroscopic characterizations and first-principle calculations, we propose that the unique Pt-Co dual sites in SAA facilitates the adsorption and dissociation of oxygen, particularly for the immobilization of OOH\* intermediate and the dissociation of OH\* intermediate, and thus result in high-efficiency four-electron ORR pathway. Consequently, the Pt<sub>1</sub>Co<sub>100</sub>/N-GCNT SAA catalyst achieves a mass activity of 0.81 A mg<sup>-1</sup><sub>Pt</sub> at 0.90 V (versus the reversible hydrogen electrode) in 0.1 M HClO<sub>4</sub> electrolyte, outperform commercial Pt/C catalyst for 5.4 times. The superior stability of the SAA catalyst was reflected by the results from the 30,000 potential-scanning cycles combined with the post characterization of the catalyst.

### 1. Introduction

While platinum (Pt)-based catalysts have been widely used as the most efficient catalysts towards speeding up ORR in proton exchange membrane fuel cells (PEMFCs), their high cost due to elemental scarcity and insufficient durability are hindering the commercialization [1–5]. Tremendous efforts were taken to improve the utilization rate of Pt and intrinsic activity of the catalysts by reducing the size of Pt nanostructures, alloying, or constructing nanostructured materials containing rich Pt surfaces [6–12]. Single-atom catalysts (SACs) are found to be significant in enhancing the utilization of metal catalysts, including single-site and dual-site catalysts [13–20]. However, most of the Pt SACs are not suitable for ORR due to their preference toward undesired two-electron (2e<sup>-</sup>) pathway to generate hydrogen peroxide (H<sub>2</sub>O<sub>2</sub>) rather than the desired four-electron (4e<sup>-</sup>) pathway for the generation of H<sub>2</sub>O, which hampers the efficiency of PEMFCs to a large extent [21–26]. Most Pt SACs are coordinated with highly electronegative elements

(such as N, S, O), and it is therefore believed that the positively-charged Pt centers may induce unfavorable adsorption of O<sub>2</sub> molecules and thus suppress their dissociation [18], which, however, is not supported by theoretical calculations [27]. The switching from the 2e<sup>-</sup> to 4e<sup>-</sup> pathway highly relies on the stable adsorption of OOH\* intermediates, which promotes the breakage of the O-O dimer rather than the protonation of OOH\* to produce H<sub>2</sub>O<sub>2</sub>. Therefore, an ideal Pt SAC should effectively facilitate O<sub>2</sub> adsorption and subsequent dissociation dynamics; however, the currently reported SACs mainly involve single Pt atom coordinated with various electronegative ligands and whose selectivity of oxygen reduction is not controllable.

Single-atom alloys (SAAs) are a new type of heterogeneous catalysts with well-defined active sites that offer a promising solution to address this challenge [28–33]. Diluting Pt atoms with inexpensive host metal atoms not only yields single-atom Pt sites but also tailors the electronic and geometric structure of the material. By delicately choosing the host metal and tuning the local atomic structure, it is viable to design a

\* Corresponding authors.

E-mail addresses: lhy06@bjut.edu.cn (H. Li), chenge@bjut.edu.cn (G. Chen), jiujun@shaw.ca (J. Zhang).

unique single-atom alloy (SAA) catalyst possessing high ORR activity. Since Pt-Co alloy is a benchmark catalyst towards the enhancement of ORR under acidic conditions [12,34–36], it would be encouraging to develop SAAs with Pt-Co dual sites, as a proof of concept, to accelerate O<sub>2</sub> adsorption and dissociation, and thus lead to a highly efficient 4e<sup>-</sup> ORR pathway by circumventing the undesired 2e- pathway resulting from most of the Pt SACs.

As initiated by above considerations, herein, several Pt<sub>1</sub>Co<sub>n</sub> alloy ( $n = 20, 50, 100$  or  $150$ ) encapsulated within N-doped graphite carbon nanotubes (N-GCNT) (expressed as Pt<sub>1</sub>Co<sub>n</sub>/N-GCNT) were successfully synthesized for their potential application as SAAs (namely, Pt<sub>1</sub>Co<sub>100</sub>/N-GCNT and Pt<sub>1</sub>Co<sub>150</sub>/N-GCNT). In 0.1 M HClO<sub>4</sub> electrolyte, the Pt<sub>1</sub>Co<sub>100</sub>/N-GCNT SAA catalyst showed remarkable catalytic ORR activity with a mass activity nearly 5.4 times higher than that of commercial Pt/C catalyst at 0.9 V vs. RHE. The high activity is believed to have originated from unique Pt-Co dual sites in SAA which creates delocalized charge and helps to adsorb and tune the dissociation energy of oxygen, endowing the key intermediates to be adsorbed and desorbed facilely over the dual sites. Meanwhile, the superiority of this catalyst was embodied in their excellent stability and barely faded activity even after 30,000 potential-scanning cycles, as a result of the unique N-GCNT encapsulating structure protecting the SAA from being corroded by acidic medium.

## 2. Experimental section

### 2.1. Chemicals

Melamine (99.5%) was purchased from Tianjin Fuchen Chemical Reagents Co., Ltd. Cobalt (II) acetate tetrahydrate (C<sub>4</sub>H<sub>6</sub>CoO<sub>4</sub>·4H<sub>2</sub>O) (99.55%) was from Aladdin. Chloroplatinic acid hexahydrate (H<sub>2</sub>PtCl<sub>6</sub>·6H<sub>2</sub>O, ≥37%) was from Sinopharm Chemical Reagent Co., Ltd. Pt/C (20 wt%) and Nafion® solution (5 wt%) were obtained from Alfa Aesar.

### 2.2. Catalyst synthesis

Melamine was first dissolved in 3 ml of DI water at 80°C with 1 mmol of C<sub>4</sub>H<sub>6</sub>CoO<sub>4</sub>·4H<sub>2</sub>O and 0.01 mmol of H<sub>2</sub>PtCl<sub>6</sub>·6H<sub>2</sub>O added. The mixture solution was stirred at room temperature for 30 min to make more uniform. The homogeneous mixture solution was then freeze-dried overnight to form purple powder. Then the powder was heated in a furnace tube from room temperature to 800 °C, with a rate of 5 °C min<sup>-1</sup>, and the temperature was kept 800 °C for 2 h in a N<sub>2</sub> atmosphere. When cooling to the room temperature, the obtained material needs to remove the excess metal particles on the outside of the carbon nanotubes in 3 M HCl solution for 2 h. Then washed the sample with DI water to neutral and freeze-dried overnight to obtain the Pt<sub>1</sub>Co<sub>100</sub>/N-GCNT catalyst. For comparison, Co/N-GCNT and Pt<sub>1</sub>Co<sub>n</sub>/N-GCNT with different mole ratios of 1:20, 1:50 and 1:150 were also synthesized by the similar procedure.

### 2.3. Characterization

The crystallinity and structures of all prepared samples were investigated using X-ray diffraction (XRD, Bruker D8 Advance X-ray diffractometer, Cu K $\alpha$ ). The morphologies of the catalysts were characterized by transmission electron microscopy (TEM, TECNAI-F20), and further to detect the elemental distribution with the EDX elemental mapping. To investigate the single Pt atoms that on the Co particles, HAADF-STEM images were observed using a Cs (image)-corrected TEM (FEI Titan G2 microscope operated at 300 kV). The detailed elemental analysis of the electrocatalysts were obtained by XPS (AXIS Supra, instrument from Kratos Analytical Ltd., Al K $\alpha$  radiation). ICP-AES (IRIS Intrepid ER/S, Thermo Elemental) was used to determine the content of Pt. The BET method was used to quantify the specific surface area by liquid nitrogen

cryosorption (Autosorb, Quantachrome, USA). The Raman microscope (LabRAM ARAMIS) involved in this article with 532 nm line of an Ar ion laser as an excitation source.

### 2.4. XAS measurements

All the XAS measurements of the Pt L<sub>3</sub>-edge and Co K-edge were detected at 1W1B beamline of Beijing Synchrotron Radiation Facility (BSRF). We used the standard samples of Co foil and Pt foil to correct the energy position. All the XAS spectra were analyzed using the Athena module implemented in the IFEFFIT software package [37]. The soft XAS data contained Co L-edge, C K-edge and N K-edge spectra in this article were conducted on 4B7B beamline of the BSRF.

### 2.5. Operando XAS measurements

The *operando* XAS experiment were conducted at the BSRF (1W1B beamline) in fluorescence mode using a Lytle detector at room temperature. For *operando* XAS measurements, an electrochemical workstation (CHI 660E) and a homebuilt cell were used. The electrolyte of 0.1 M HClO<sub>4</sub>, carbon paper supported with catalyst, carbon rod and Hg/HgSO<sub>4</sub> were used as the working, counter and reference electrodes, respectively. In XAS measurements, Pt foil was used to calibrate the position of the absorption edge (E<sub>0</sub>), and all XAS data were collected within one beam time. In order to monitor the change of XAS spectrum in ORR process, we applied 0.9 V ~ 0.3 V potential relative to RHE to the cathode in 0.1 M HClO<sub>4</sub> for data acquisition. Before collecting the signal data, the different applied potential was maintained for 5 min to make a steady state.

### 2.6. Electrochemical measurements

All the electrochemical measurements were performed in a conventional three-electrode configuration at room temperature using the BioLogic VMP3 electrochemical workstation. All tests were performed using a three-electrode system including of a working electrode of rotating disk electrode (RDE, 5 mm in diameter, from the PINE instrument), Hg/Hg<sub>2</sub>SO<sub>4</sub> and carbon rod as the reference and counter electrode. In order to prepare a uniform catalyst ink, 2 mg of catalyst powder was dispersed in a mixture solution contains 290  $\mu$ l isopropyl alcohol and 700  $\mu$ l of DI water, and 10  $\mu$ l of Nafion® solution (Alfa Aesar, 5 wt%) was added and ultrasonicated for 30 min. Then 10  $\mu$ l prepared catalyst ink was dropped on the polished RDE electrode, and the electrode was dried at room temperature to make a thin film. All the potentials related in this study were corrected to reversible hydrogen electrode (RHE). For cyclic voltammetry (CV) tests, the working electrode was tested in N<sub>2</sub> and O<sub>2</sub> at a sweep rate of 50 mV s<sup>-1</sup> (scan range 0.1–1.1 V vs. RHE). According to the current density and peak potential of the recorded current voltage curves, the catalytic performance of the catalyst was evaluated. In the RDE test, the polarization curves were conducted in 0.1 M HClO<sub>4</sub> solution with O<sub>2</sub>-saturated at a scanning rate of 10 mV s<sup>-1</sup> and the rotating speed was varied from 400 rpm to 2500 rpm. Ohmic compensation in the test was realized by ZIR module in EC Lab software. The reference value for the voltage setting was the potential at the beginning of the linear sweep voltammetry (LSV) scan when the limiting diffusion current was reached. The percentage of ohmic compensation was 85% potential, the amplitude was 10 mV, and the pulse frequency was 100 kHz. The resistance value obtained at this pulse frequency could be approximately considered to be consistent with the actual resistance value.

The kinetic process of oxygen reduction can be analyzed and evaluated by the Koutecky-Levich (K-L) equation. The diffusion current in the platform region presents a function relationship with the rotational speed of the RDE, which can be expressed as:

$$\frac{1}{J} = \frac{1}{J_L} + \frac{1}{J_K} = \frac{1}{B\omega^{1/2}} + \frac{1}{J_K} \quad (1)$$

Where  $J$  represents the measured current density;  $J_L$  and  $J_K$  are the diffusion limiting and kinetic current densities, respectively; and  $\omega$  is the angular velocity. In this work, the K-L curves was used to determine the values of  $B$  (the inverse of the slope  $k$ ). The number of electrons transferred by each oxygen molecule in ORR reaction were obtained according the following formula:

$$B = 0.2nFC_0(D_0)^{2/3}v^{-1/6} \quad (2)$$

Where  $n$  is the electron transfer number;  $F$  is the Faraday constant ( $96,485 \text{ C mol}^{-1}$ );  $C_0$  is the bulk concentration of  $\text{O}_2$  ( $1.2 \times 10^{-3} \text{ mol L}^{-1}$ );  $D_0$  is the diffusion coefficient of  $\text{O}_2$  ( $1.9 \times 10^{-5} \text{ cm}^2 \text{ s}^{-1}$ );  $v$  and  $k$  represent the kinematic viscosity of the electrolyte ( $0.01 \text{ cm}^2 \text{ s}^{-1}$ ) and electron-transfer rate constant, respectively. For Tafel plots, the kinetic current was calculated by the mass transport correction of RDE.

$$J_K = \frac{J \times J_L}{J_L - J} \quad (3)$$

The rotating ring-disk electrode (RRDE) test was recorded at a scan rate of  $10 \text{ mV s}^{-1}$  in an  $\text{O}_2$ -saturated  $0.1 \text{ M HClO}_4$  electrolyte. The ring electrode potential was set to  $+1.20 \text{ V}$  vs. RHE. The electron transfer number ( $n$ ) and the percentage of  $\text{HO}_2^-$  were calculated by the following equations:

$$\text{HO}_2^- \% = 200 \times I_R / ((N \times |I_D| + I_R)) \quad (4)$$

$$n = 4 \times |I_D| / (|I_D| + |I_R| / N) \quad (5)$$

Where  $I_D$  is the disk current,  $I_R$  is the ring current, the collection efficiency ( $N$ ) of the Pt ring was measured to be 0.37 here.

The accelerated durability test (ADT) was tested by running 30,000 cycles in  $0.1 \text{ M HClO}_4$  solution with  $\text{O}_2$ -saturated at a voltage range of  $0.6\text{--}1.0 \text{ V}$  vs. RHE at a scan rate of  $200 \text{ mV s}^{-1}$ . After stability test, the catalyst on the working electrode was ultrasonically collected by ethanol for further structure and composition analysis.

## 2.7. Calculation method

All the first principle DFT calculations were operated using Vienna Ab initio Simulation Package (VASP) [38] in a projector augmented wave (PAW) method [39]. The exchange-functional was treated by the generalized gradient approximation (GGA) of Perdew-Burke-Ernzerhof (PBE) [40] functional. The Spin-polarizations were carried out for all calculations. A  $450 \text{ eV}$  energy cutoff for the plane wave basis expansion was used, while a less than  $0.03 \text{ eV}/\text{\AA}$  force on each atom was set to assess the convergence of geometry relaxation. A  $2 \times 2 \times 1$  k-point mesh sampling was used for the Brillouin zone integration. The convergence energy threshold was set to be  $10^{-4} \text{ eV}$  for self-consistent calculations. The DFT-D3 method was used to consider the van der Waals interaction [41]. The interaction between periodic structures was avoided by adding a  $15 \text{ \AA}$  vacuum along the Z direction.

The free energies of the ORR steps were calculated using the following equation: [42].

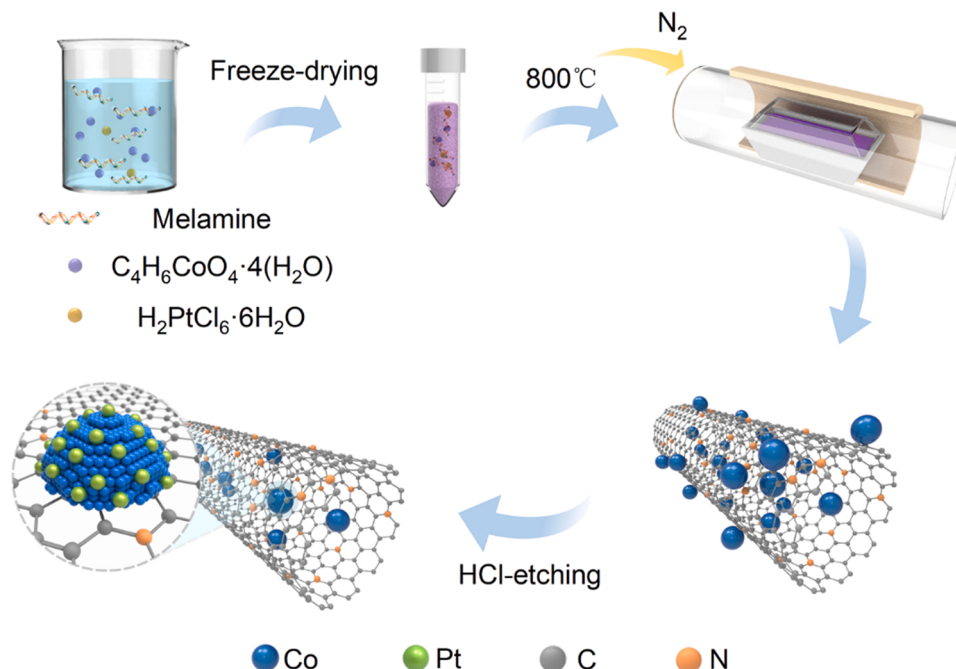
$$\Delta G = \Delta E_{\text{DFT}} + \Delta E_{\text{ZPE}} - T\Delta S \quad (6)$$

Where  $\Delta E_{\text{DFT}}$  is the DFT energy difference, and  $\Delta E_{\text{ZPE}}$  and  $T\Delta S$  terms were obtained based on vibration analysis.

## 3. Results and discussion

### 3.1. Synthesis and characterization

The  $\text{Pt}_1\text{Co}_n/\text{N-GCNT}$  was synthesized by the melamine pyrolysis method (Scheme 1, details in the experimental section). Different molar ratios of Pt-Co alloys, namely  $\text{Pt}_1\text{Co}_{20}/\text{N-GCNT}$ ,  $\text{Pt}_1\text{Co}_{50}/\text{N-GCNT}$ ,  $\text{Pt}_1\text{Co}_{100}/\text{N-GCNT}$ ,  $\text{Pt}_1\text{Co}_{150}/\text{N-GCNT}$  and  $\text{Co}/\text{N-GCNT}$ , were synthesized to conduct a comparative study. Fig. 1a displays the XRD results of the prepared catalysts. All samples can be well identified to have a crystallized Co metal diffraction peaks, as referenced by the standard pattern (JCPDS, No. 15–0806). A typical peak situated at  $26.4^\circ$  was indexed as (002) facet of graphitic carbon. The graphitic carbon peak of the  $\text{Co}/\text{N-GCNT}$  sample is weaker than that of  $\text{Pt}_1\text{Co}_n/\text{N-GCNT}$ , indicating that the introduction of Pt species leads to a higher degree of



**Scheme 1.** The schematic for the synthetic process of  $\text{Pt}_1\text{Co}_n/\text{N-GCNT}$  encapsulated in a graphitic carbon nanotube. The gray, orange, blue, and green atoms represent carbon, nitrogen, cobalt, and platinum atoms, respectively.

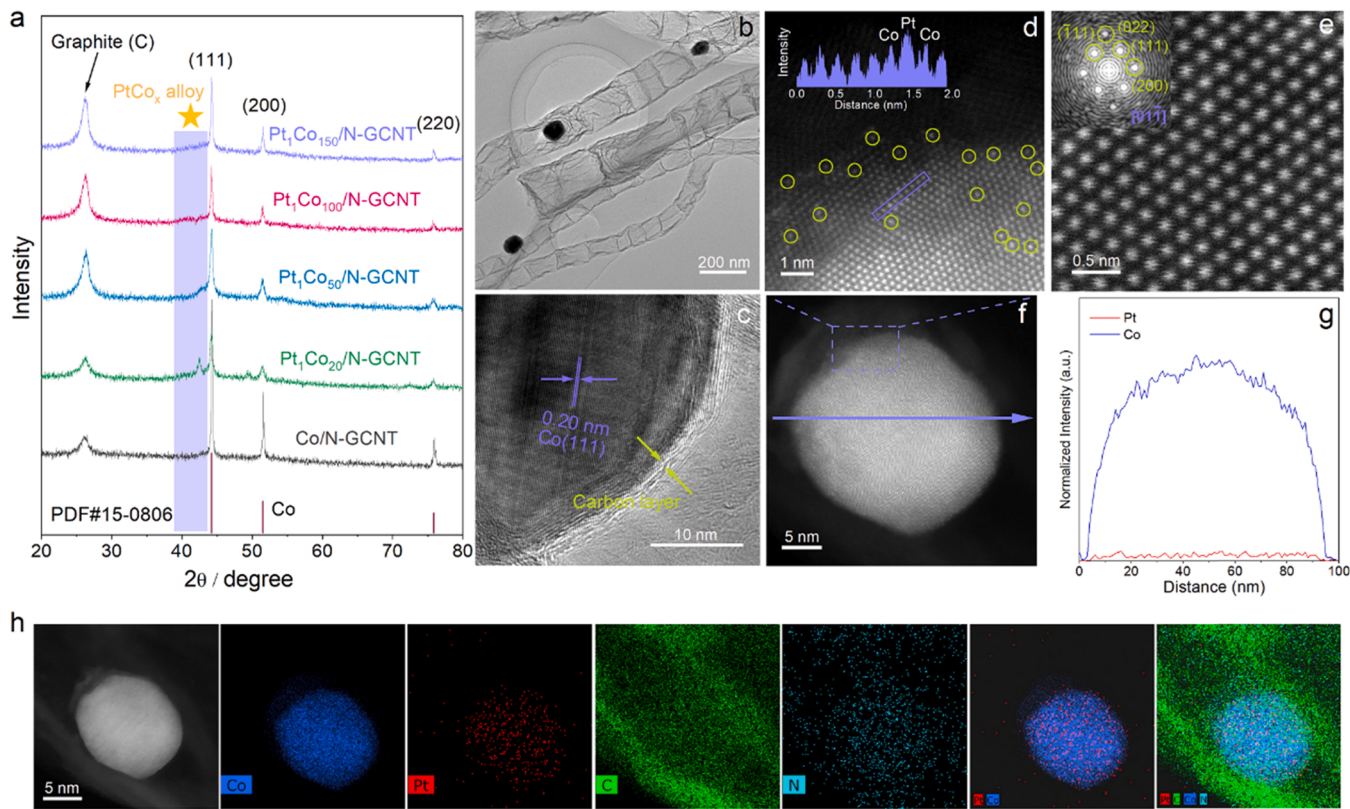


**Fig. 1.** (a) XRD results for different  $\text{Pt}_1\text{Co}_n/\text{N-GCNT}$  catalysts ( $n = 20, 50, 100$ , and  $150$ ). (b) (c) TEM as well as HRTEM images of  $\text{Pt}_1\text{Co}_{100}/\text{N-GCNT}$ . (d) (e) HAADF-STEM image of  $\text{Pt}_1\text{Co}_{100}/\text{N-GCNT}$ . The insert in (d) displays the line-scan intensity profile obtained from the purple box. The inset in (e) shows correspondingly the SAED pattern. (f) HAADF-STEM image of  $\text{Pt}_1\text{Co}_{100}/\text{N-GCNT}$ . The purple line is the line scan across  $\text{Pt}_1\text{Co}_{100}/\text{N-GCNT}$ . (g) The corresponding line scan profile from (f). (h) STEM-EDS elemental mapping of  $\text{Pt}_1\text{Co}_{100}/\text{N-GCNT}$ .

graphitization of the CNTs. Notably, a peak around  $43^\circ$  can be easily noticed in the patterns of  $\text{Pt}_1\text{Co}_{20}/\text{N-GNT}$ , indicative of the formation of  $\text{PtCo}_x$  alloy particles. However, with decreasing content of Pt, this characteristic peak is weakened and finally vanished at  $\text{Pt}_1\text{Co}_{100}/\text{N-GCNT}$  and  $\text{Pt}_1\text{Co}_{150}/\text{N-GCNT}$ . The Pt content in  $\text{Pt}_1\text{Co}_{100}/\text{N-GCNT}$  was determined to be 1.9 wt% assisted by the inductively coupled plasma optical emission spectrometry (ICP-OES).

The transmission electron microscopy (TEM) was employed to investigate the structures and morphologies of the Co/N-GCNT and  $\text{Pt}_1\text{Co}_{100}/\text{N-GCNT}$  samples. Initially, the low-magnification TEM figures of both Co/N-GCNT and  $\text{Pt}_1\text{Co}_{100}/\text{N-GCNT}$  show the metal particles of  $\sim 100$  nm and are encapsulated in bamboo-shaped carbon nanotubes with a diameter of  $100\text{--}200$  nm (Fig. 1b, Fig. S1 and S2). Fig. 1c shows high-resolution transmission electron microscopy (HRTEM) results, in which one can observe that the particles possess a lattice distance of  $\sim 0.2$  nm that can be indexed as the (111) plane of Co metal phase, well consistent with previous XRD results. A 2 nm-thick carbon layer can be clearly observed in capsulating the Co nanoparticles. However, no trace of Pt particles were detected. The HAADF-STEM was further employed to examine the exact form of Pt existence. As shown in Fig. 1d, the existence of Pt single atoms dispersed on Co surface can be inferred from the yellow circle marked brighter spots, which are atomic number sensitive. Then the line-scan elemental profile in Fig. 1d were used to verify the atomic dispersion of the isolated Pt, where a distinct higher intensity can be spotted. Further analysis of the atomic phase (Fig. 1e) demonstrates no distortion and crystal lattice variation, suggesting the absence of structural change caused by the introduction of Pt. In addition, the line scan on a single particle (Fig. 1f) indicated by the purple arrow unambiguously reveals the presence of trace amounts of Pt in contrast to Co, signifying the existence of atomic Pt rather than  $\text{PtCo}$  alloy or Pt particles (Fig. 1g). Moreover, the STEM-coupled EDS element mapping

further validated the presence of Pt, Co, C, and N elements and uniform distribution of Pt on Co particles, as well as the successful encapsulation of  $\text{Pt}_1\text{Co}_{100}$  particle in nitrogen doped graphitized carbon nanotubes (Fig. 1h, Fig. S3). For comparison, the TEM and EDS images of the other samples containing different Pt: Co molar ratios were obtained. Fig. S4-S5 suggest that the formation of carbon nanotubes is not uniform due to agglomeration in some regions with the increasing Pt content, revealing the essentiality of low Pt content for maintaining the unique architecture. With the Pt: Co ratio of 1:150 (Fig. S6), the particles give exclusive Co elemental information while the existence of Pt was hardly detectable.

The Brunauer–Emmett–Teller (BET) test was performed for  $\text{Pt}_1\text{Co}_{100}/\text{N-GCNT}$ . The results give a type-IV nitrogen adsorption-desorption isotherm, indicating the existence of a mesoporous structure (Fig. S7a, S7b). By comparing the BET data of  $\text{Pt}_1\text{Co}_{100}/\text{N-GCNT}$  and Co/N-GCNT shown in Fig. S8, we found that there is no significant difference between them, indicating that the introduction of a small amount of Pt will not have a great influence on carbon nanotubes. The increased  $I_D/I_G$  ratio from Co/N-GCNT to  $\text{Pt}_1\text{Co}_{100}/\text{N-GCNT}$  in the Raman spectra (Fig. S9) suggests an enhanced graphitization of CNTs with the existence of Pt species, in good consistency with previous XRD results. The high graphitization of CNTs, porosity, and large BET surface area ( $155 \text{ m}^2 \text{ g}^{-1}$ ) are beneficial to enhance the number of active sites on  $\text{Pt}_1\text{Co}_{100}/\text{N-GCNT}$  and favor mass transfer during the electrocatalysis.

The local and electronic structure of  $\text{Pt}_1\text{Co}_{100}/\text{N-GCNT}$  was further investigated by X-ray absorption spectroscopy (XAS) technique. Fig. 2a shows Pt L<sub>3</sub>-edge XANES of different samples, where the intensity of the white-line peak is close to that of the Pt foil, demonstrating the presence of the metallic Pt species [43]. The Fourier transformed (FT) extended X-ray absorption fine structure (EXAFS) was further used to pinpoint the local environment of Pt [44]. Fig. 2b displays the main peak at  $2.2 \text{ \AA}$  in

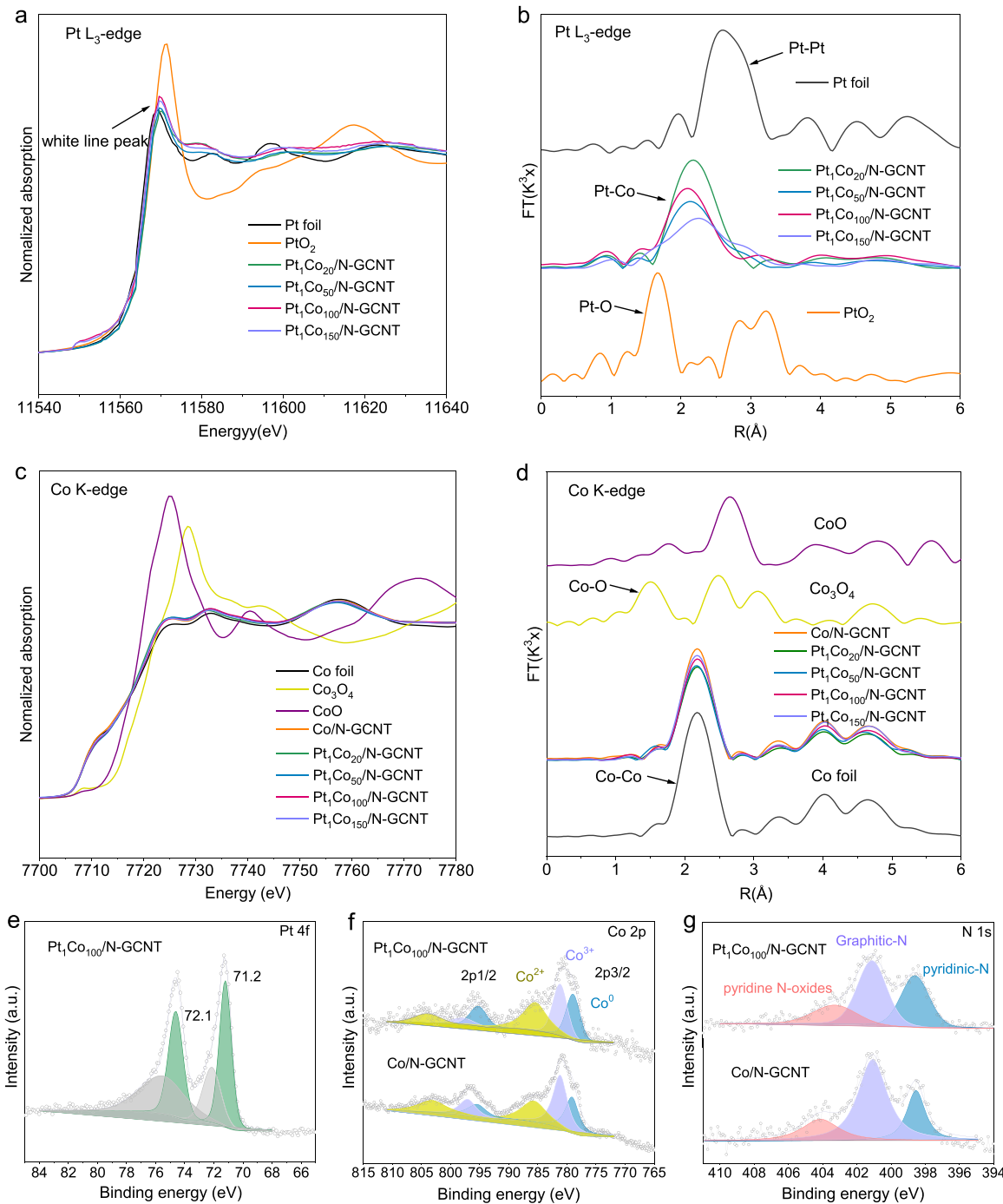


**Fig. 2.** (a) Normalized Pt L<sub>3</sub>-edge XANES spectra of Pt foil, PtO<sub>2</sub>, Pt<sub>1</sub>Co<sub>20</sub>/N-GCNT, Pt<sub>1</sub>Co<sub>50</sub>/N-GCNT, Pt<sub>1</sub>Co<sub>100</sub>/N-GCNT and Pt<sub>1</sub>Co<sub>150</sub>/N-GCNT. (b) Fourier-transformed EXAFS spectra at the Pt L<sub>3</sub>-edge. (c) Co K-edge XANES spectra of Co foil, Co<sub>3</sub>O<sub>4</sub>, CoO, Pt<sub>1</sub>Co<sub>20</sub>/N-GCNT, Pt<sub>1</sub>Co<sub>50</sub>/N-GCNT, Pt<sub>1</sub>Co<sub>100</sub>/N-GCNT and Pt<sub>1</sub>Co<sub>150</sub>/N-GCNT. (d) Fourier-transformed EXAFS spectra at the Co K-edge. (e) Pt 4 f XPS spectra of Pt<sub>1</sub>Co<sub>100</sub>/N-GCNT. (f) Co 2p (g) N 1 s XPS spectra of Co/N-GCNT and Pt<sub>1</sub>Co<sub>100</sub>/N-GCNT.

Pt<sub>1</sub>Co<sub>100</sub>/N-GCNT, which can be assigned to the first-shell Pt-Co coordination, and also the absence of Pt-Pt shell peaks at 2.6 Å and 2.75 Å being present in the FT-EXAFS curves of Pt foil and PtO<sub>2</sub>, respectively. This undoubtedly precludes the formation of Pt particles and thus indicates the formation of Pt-Co single-atom alloys. In Fig. 2c, Co K-edge XANES shows well superimposed spectra for all the samples with Co foil and Co/N-GCNT, indicating the presence of Pt does not change the electronic structure of metallic Co species. This is further corroborated by the similar Co FT-EXAFS results shown in Fig. 2d, which only exhibits a main peak at ~2.2 Å corresponding to Co-Co shell. Although the Co

K-edge XAS demonstrates no obvious change in the samples, the Co L-edge XAS (TEY mode, surface-sensitive) in Fig. S10 shows an increase in the peak intensity from Pt<sub>1</sub>Co<sub>100</sub>/N-GCNT to Co/N-GCNT, revealing the apparent charge transfer between surface Co and Pt atoms. The combinative analysis of the Pt L<sub>3</sub>-edge, Co K-edge, and L-edge XAS spectra provide competent evidence that the Pt atoms mainly stay on the surface and forming Pt<sub>1</sub>Co<sub>100</sub> single-atom alloy.

The chemical composition as well as the valence states for all the samples were further analyzed by XPS, with the full spectra shown in Fig. S11. The high-resolution Pt 4 f<sub>7/2</sub> spectrum of Pt<sub>1</sub>Co<sub>100</sub>/N-GCNT in

**Fig. 2e** (the results for other samples can be found in **Fig. S12** for comparison) shows two peaks centered at 71.2 and 72.1 eV. The peak observed at the lower binding energy of Pt 4f indicates a slightly oxidized Pt species, which is mainly caused by the formation of single atom alloy of Pt<sub>1</sub>Co<sub>100</sub>. The Co 2 P<sub>3/2</sub> spectra (**Fig. 2f** and **Fig. S13**) exhibit three peaks at around 779.3, 782.2, and 787.3 eV, respectively that can be designated as the presence of metallic Co, Co<sub>x</sub>Ny or Co-Ny, and Co-O species [32,45,46]. The higher valence states of the Co species might be caused by the electronic interaction between the N-CNTs and Co nanoparticles. In addition, the N 1 s spectra (**Fig. 2g** and **Fig. S14**) split into two peaks of 398.6 eV and 401.0 eV that can be assigned to the pyridine-N and graphitic N, respectively; the one at 404.4 eV mainly corresponds to pyridine N-oxide [47]. Also, the presence of peak A (401.3 eV) and peak B (407.3 eV) in the N K-edge XAS spectra in **Fig. S15** suggests the formation of graphite N and C-N-C or C-N σ bonds [48]. The C 1 s XPS spectra of **Fig. S16** indicates the presence of a graphite-carbon layer in Pt<sub>1</sub>Co<sub>n</sub>/N-GCNT, which is confirmed by the C K-edge XAS spectrum in **Fig. S17**.

### 3.2. Catalyst activity in ORR

The electrocatalytic ORR activity of Pt<sub>1</sub>Co<sub>100</sub>/N-GCNT was measured in 0.1 M HClO<sub>4</sub> electrolyte under room temperature. The cyclic voltammetry curves (CVs) of Pt<sub>1</sub>Co<sub>100</sub>/N-GCNT in 0.1 M HClO<sub>4</sub> solution saturated with N<sub>2</sub> and O<sub>2</sub> are presented in **Fig. 3a**. Unlike Pt/C, the Pt<sub>1</sub>Co<sub>100</sub>/N-GCNT shows no hydrogen adsorption and desorption peaks

(**Fig. S18**), serving as a further potent evidence of SAA rather than Pt particles. Obviously, Pt<sub>1</sub>Co<sub>100</sub>/N-GCNT shows a strong cathodic reduction peak at ~0.8 V in the O<sub>2</sub>-saturated HClO<sub>4</sub> solution, which is indicative of its high ORR activity. The linear sweep voltammetry (LSV) measurements of different samples were taken using the rotating disk electrode (RDE) at room temperature in an O<sub>2</sub>-saturated 0.1 M HClO<sub>4</sub> solution (**Fig. 3b**). Note that the Co/N-GCNT shows poor ORR activity, implying the Co and the N-GCNPs are not responsible for the highly efficient ORR observed in Pt<sub>1</sub>Co<sub>100</sub>/N-GCNT sample. Upon the addition of Pt, the performance of Pt<sub>1</sub>Co<sub>n</sub>/N-GCNT was significantly boosted, among which the optimum enhancement was achieved for the Pt<sub>1</sub>Co<sub>100</sub>/N-GCNT sample. The half-wave potential of Pt<sub>1</sub>Co<sub>100</sub>/N-GCNT approaches 0.85 V (vs. RHE), comparable with the commercial Pt/C catalyst. Additionally, the Tafel slope of Pt<sub>1</sub>Co<sub>100</sub>/N-GCNT is found to be 82 mV dec<sup>-1</sup> (**Fig. S19**), exhibiting fast catalytic ORR kinetics. The ORR kinetics was further explored by the electron transfer number (*n* = 4) calculated from the Koutecky-Levich (K-L) plots, suggesting the occurrence of a four-electron pathway for Pt<sub>1</sub>Co<sub>100</sub>/N-GCNT (**Figs. S20, S21**), which is consistent with the result from RRDE measurements (**Fig. S22**). In addition, we found the HO<sub>2</sub><sup>·</sup> yield was below 5% from 0.20 to 0.80 V vs. RHE, which suggest the mainly four-electron reaction for Pt<sub>1</sub>Co<sub>100</sub>/N-GCNT. Moreover, the mass activity relative to the normalized Pt mg<sup>-1</sup> was also calculated from the linear sweep voltammetry curves (LSVs) (**Fig. 3c**). The mass activity of Pt<sub>1</sub>Co<sub>100</sub>/N-GCNT is 0.81 A mg Pt<sup>-1</sup> at 0.9 V and 2.57 A mg Pt<sup>-1</sup> at 0.85 V vs. RHE, which is comparable to those of very recently reported Pt-based catalysts (**Table S1**) and

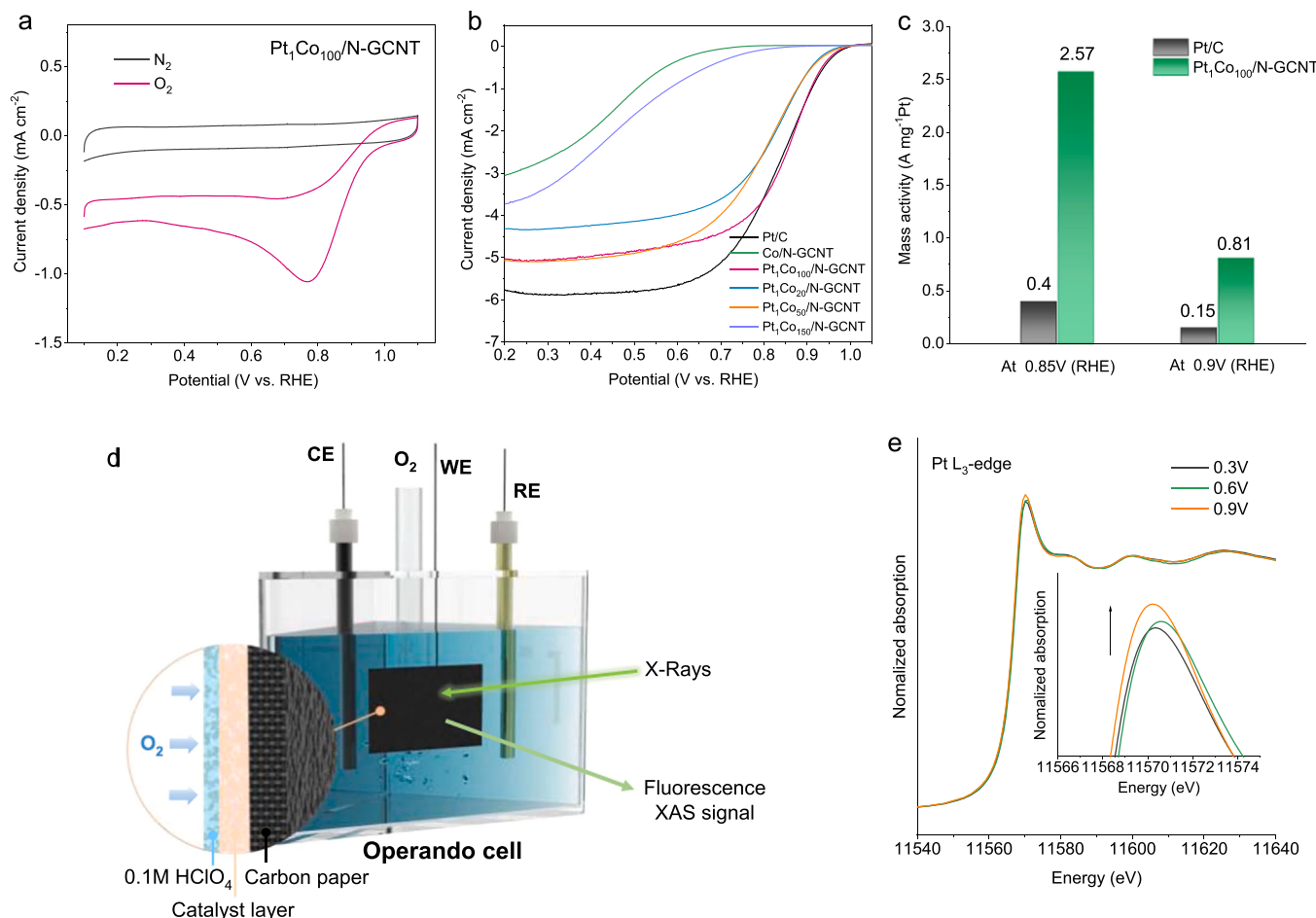


**Fig. 3.** (a) Cyclic voltammetry curves (CVs) of Pt<sub>1</sub>Co<sub>100</sub>/N-GCNT in the N<sub>2</sub>/O<sub>2</sub>-saturated 0.1 M HClO<sub>4</sub> electrolyte at the scan rate of 50 mV s<sup>-1</sup>. (b) ORR polarization curves of Pt/C (20 wt%), Co/N-GCNT, Pt<sub>1</sub>Co<sub>20</sub>/N-GCNT, Pt<sub>1</sub>Co<sub>50</sub>/N-GCNT, Pt<sub>1</sub>Co<sub>100</sub>/N-GCNT, Pt<sub>1</sub>Co<sub>150</sub>/N-GCNT recorded in the O<sub>2</sub>-saturated 0.1 M HClO<sub>4</sub> electrolyte at the scan rate of 10 mV s<sup>-1</sup> and a rotation rate of 1600 rpm, respectively. (c) Mass activities (MA) of Pt/C (20 wt%) and Pt<sub>1</sub>Co<sub>100</sub>/N-GCNT at 0.85 V and 0.9 V (vs. RHE). (d) Schematic representation of the *Operando* Pt L<sub>3</sub>-edge XANES setup. (e) *Operando* Pt L<sub>3</sub>-edge XANES spectra of Pt<sub>1</sub>Co<sub>100</sub>/N-GCNT with the peak area enlarged.

outperform the value obtained for commercial Pt/C catalyst by 5.4 and 6.4 times, respectively.

*Operando* XAFS measurements were conducted to get insights into the active sites of Pt<sub>1</sub>Co<sub>100</sub>/N-GCNT catalyst during the ORR process. The setup of the *Operando* XAS experiments performed under the fluorescence mode is schematically shown in Fig. 3d, where a three-electrode system with a gas diffusion electrode is inserted into a homemade *Operando* cell in order to perform the test. The Pt L<sub>3</sub>-edge XANES spectra of Pt<sub>1</sub>Co<sub>100</sub>/N-GCNT were collected at the applied potentials of 0.3, 0.6, and 0.9 V (vs. RHE), respectively, as can be seen in Fig. 3e. The normalized white-line peak intensity increases with increasing applied potential, suggesting the chemisorption of the oxygenated species on Pt [10]. The EXAFS results at different potentials in Fig. S23 show similar profiles, indicating a stable Pt atomic structure during the ORR process. To summarize, the Pt<sub>1</sub>Co<sub>100</sub>/N-GCNT demonstrates high 4e- ORR performance under acidic conditions, which is assumed to originate from the unique Pt-Co dual sites in SAA.

### 3.3. Stability of the catalyst in ORR

The electrochemical stability of the Pt<sub>1</sub>Co<sub>100</sub>/N-GCNT catalyst was further evaluated by the accelerated durability test (ADT), which was performed by potential cycling performed in the voltage range of 0.6~1.0 V (vs. RHE). As shown in Fig. 4a, Pt<sub>1</sub>Co<sub>100</sub>/N-GCNT shows a negligible change in the polarization curves after the 30,000 cycles of ADT, while the degradation of commercial Pt/C catalyst is much greater (Fig. S24). To investigate the change of morphology and microstructure of Pt<sub>1</sub>Co<sub>100</sub>/N-GCNT after ADT, we have conducted the post characterization of catalyst. As shown in Fig. S25, the TEM image shows that the morphology of Pt<sub>1</sub>Co<sub>100</sub>/N-GCNT remains intact while Pt/C displays severe aggregation (Fig. S26). The Pt atom still exists in the form of single atom on the surface of the Co particles, highlighting its highly stable atomic structure. The line scanning suggests that Pt is evenly dispersed on the Co particles (Fig. 4b and c), and the encapsulated Pt<sub>1</sub>Co<sub>100</sub> nanoparticles show the homogeneous elemental distribution

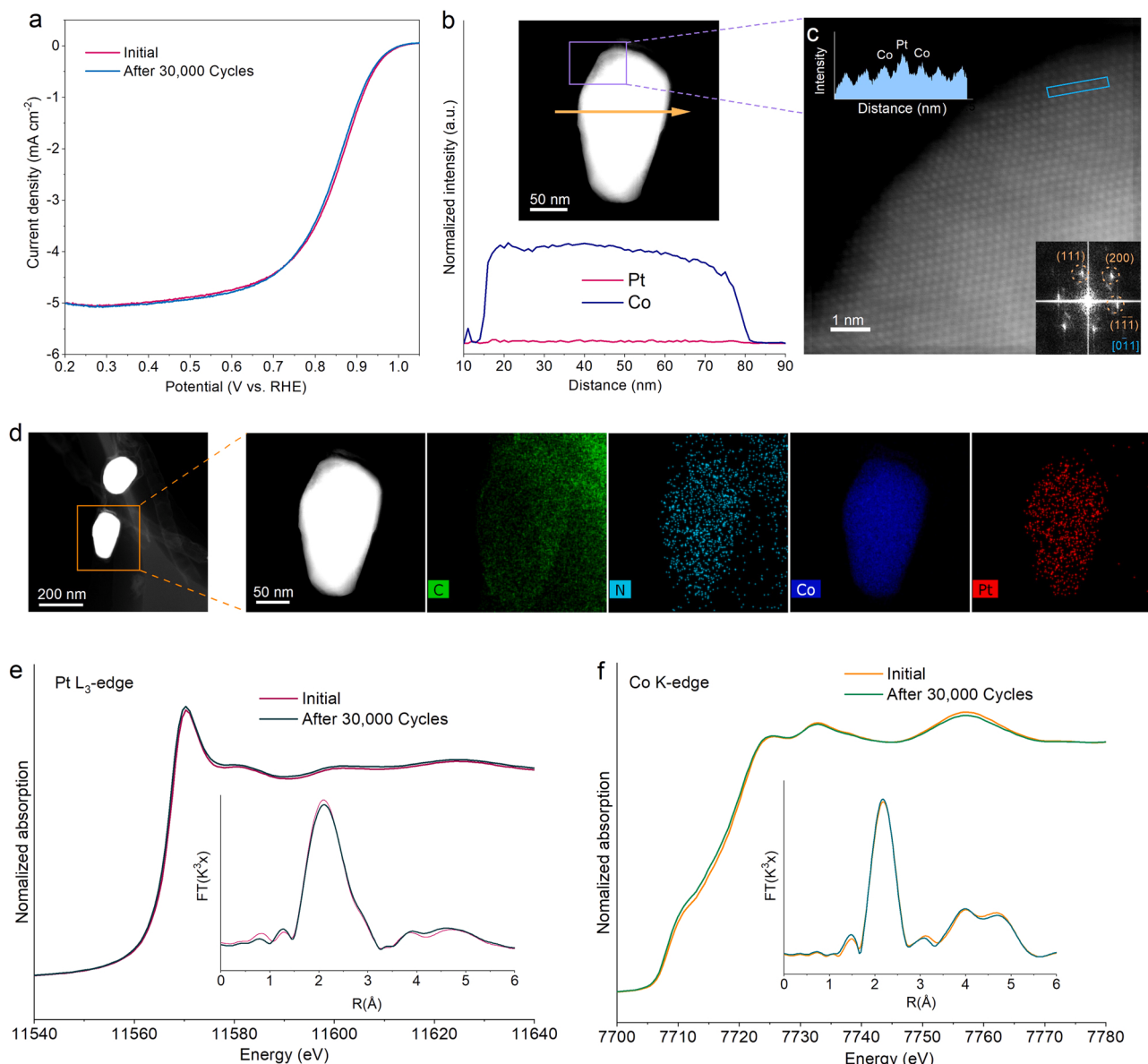


**Fig. 4.** (a) RDE (rotating disk electrode) potential cycling stability test for Pt<sub>1</sub>Co<sub>100</sub>/N-GCNT from 0.6 to 1.0 V (vs. RHE) at a scan rate of 200 mV s<sup>-1</sup>. (b) Line-scans of HAADF-STEM image (d) EDS-mappings of Pt<sub>1</sub>Co<sub>100</sub>/N-GCNT after potential cycling of 30,000 cycles. (e) Pt L<sub>3</sub>-edge XANES spectra of Pt<sub>1</sub>Co<sub>100</sub>/N-GCNT. The insert of (e) displays the Fourier-transformed EXAFS spectra at Pt L<sub>3</sub>-edge. (f) Co K-edge XANES spectra of Pt<sub>1</sub>Co<sub>100</sub>/N-GCNT. The insert of (f) shows the Fourier-transformed EXAFS spectra at the Co K-edge.

(Fig. 4d). Meanwhile, Pt L<sub>3</sub>-edge and Co K-edge XAS of Pt<sub>1</sub>Co<sub>100</sub>/N-GCNT sample after ADT was further collected. Fig. 4e and f show that the XANES and EXAFS results of Pt<sub>1</sub>Co<sub>100</sub>/N-GCNT have slight change variations from the fresh sample, revealing the stability of the chemical state of Pt and Co species in Pt<sub>1</sub>Co<sub>100</sub>/N-GCNT, except that some minor reduction of Co happened in the very surface area as taken by the XPS analysis (Fig. S27). In addition, the Raman spectra (Fig. S28) suggests that the graphitized carbon nanotubes possess the same basic structure as that of the sample before the ADT process. Therefore, the 30,000 potential-scanning cycles testing combined with post characterization of Pt<sub>1</sub>Co<sub>100</sub>/N-GCNT catalyst exhibits its superior stability, which could be attributed to the graphitized carbon layer protecting the SAA from leaching and agglomeration. Moreover, such excellent stability hints the Pt<sub>1</sub>Co<sub>100</sub>/N-GCNT catalyst has distinct actives sites, i.e. the synergistic Pt-Co site as uncovered later by DFT calculations, compared with that of pure Pt or Co sites in specific catalysts.

### 3.4. Theoretical investigation

DFT calculations were performed to shed more light on the superior ORR activity of Pt<sub>1</sub>Co<sub>100</sub>/N-GCNT. Initially, a representative PtN<sub>4</sub>/Graphene (PtN<sub>4</sub>/G) structure was chosen to identify why a general single Pt atom catalyst exhibits a poor catalytic performance toward the 4e-ORR process. (Fig. S29). From the density of states (DOS) presented in Fig. S33, the Pt 5d states in PtN<sub>4</sub>/G are lying deeply from the Fermi level due to the strong electronegativity of N adsorbing charge from Pt 5d, resulting in poor oxo-philicity of the Pt center. As shown in Fig. S30, the calculated free-energy diagram shows even a positive energy change indicating energetically unfavorable adsorption of the OOH\* intermediates, implying a preferred 2e- ORR process. (The intermediate adsorption model and mechanistic diagram are shown in Fig. S31 and S32). The results indicate that most of the single Pt atoms, as represented by PtN<sub>4</sub>/G, are unable to effectively adsorb oxygen and stabilize the OOH\* intermediates.

The Pt<sub>1</sub>Co<sub>100</sub>/N-GCNT model was then built by substituting a surface Co atom from the most stable Co (111) facet with a Pt atom, followed by coating with an N-doped carbon layer (Fig. 5a). Fig. 5b shows the free-energy paths of the intermediates involved in ORR with Pt<sub>1</sub>Co<sub>100</sub>/N-GCNT. Initially, we calculated the ORR reaction on Co surface for the purpose of comparison. We found that the OOH\* species, once absorbed on Co surface, will directly decompose into OH\* and O\* species as unambiguously observed from the optimized structure (Fig. S34). Worth mentioning is that the limited ORR performance of Co/N-GCNT may partially originate from some undetectable species (e.g. Co-N<sub>x</sub>) [49,50] but whose current contribution is small compared with that of Pt<sub>1</sub>Co<sub>100</sub>/N-GCNT in the potential range of 0.6–1.0 V (vs. RHE), as shown in Fig. 3b. In contrast, the steps for Pt<sub>1</sub>Co<sub>100</sub>/N-GCNT share a much-averaged free energy change, indicative of the excellent balance of the adsorption and desorption of the intermediates, which explains the superior ORR performance of the catalyst. The DFT optimized crystal structures of different intermediates are presented in Fig. 5c. Unlike the Pt single atom site in PtN<sub>4</sub>/G, the Pt-Co dual sites adsorption mode is more beneficial for the stabilization of the OOH\* intermediate (Fig. S30). The stable OOH\* adsorption leads to the easy cleavage of the O-O bond in the subsequent steps. The higher oxo-philicity of the Pt-Co dual sites is attributed to the more delocalized Pt 5d electrons in Pt<sub>1</sub>Co<sub>100</sub>/N-GCNT; compared with high electronegative N atom, the less electronegativity of Co atom moderately tunes Pt electronic structure (Fig. S33). Note that the comparison of Pt<sub>1</sub>Co<sub>100</sub> alloy and Pt<sub>1</sub>Co<sub>100</sub>/N-GCNT in Fig. S35 indicates that the presence or absence of nitrogen-doped graphene has negligible effect on ORR activity with similar free-energy diagram of the ORR pathways and the same intermediate adsorption structure (Fig. S36).

To reveal the essentiality of Pt-Co dual sites in tuning the adsorption of oxygenated species, the ORR free energy change diagram for the Pt-Pt dual sites adsorption is also calculated, as a comparison, by replacing the

two neighboring Co with Pt atoms (Pt<sub>2</sub>Co<sub>100</sub>/N-GCNT in Fig. 5b with the model shown in Fig. S37). It unambiguously displays a lower energy change during the first step along with the formation of OOH\* intermediate, highlighting its rate-limiting nature (Fig. S38 shows different intermediates). The worsening of OOH\* adsorption for Pt<sub>2</sub>Co<sub>100</sub> may be partially nested in the subtle electronic interactions between the two Pt atoms. The charge density difference as well as density of states (Fig. S39, S40) suggests a relatively lower d band center for Pt<sub>2</sub>Co<sub>100</sub>/N-GCNT than Pt<sub>1</sub>Co<sub>100</sub>/N-GCNT, reflecting the superiority of Pt-Co in the immobilization of the OOH\* intermediates. In addition, the OH\* desorption energy of Pt<sub>2</sub>Co<sub>100</sub>/N-GCNT is larger than that of Pt<sub>1</sub>Co<sub>100</sub>/N-GCNT. The optimized structure reveals the OH\* intermediate is adsorbed on the two adjacent Pt atoms in a bridge type for Pt<sub>2</sub>Co<sub>100</sub>/N-GCNT rather than end-on adsorption as observed in Pt<sub>1</sub>Co<sub>100</sub>/N-GCNT (Fig. S38). This bridge adsorption mode is not beneficial for the dissociation of OH\*, hence requiring larger dissociation energy. The proposed mechanisms for Pt<sub>1</sub>Co<sub>100</sub>/N-GCNT and Pt<sub>2</sub>Co<sub>100</sub>/N-GCNT are finally schematically presented in Fig. 5d & 5e. To summarize, the unique Pt-Co dual sites in Pt<sub>1</sub>Co<sub>100</sub>/N-GCNT facilitates the immobilization of OOH\* intermediate and the dissociation of OH\* intermediate, and thus, result in a highly efficient 4e- ORR pathway. Therefore, an appropriate amount of Pt alloying with Co is crucial for the achievement of an optimal activity. The Pt atoms are prone to cluster together upon further addition onto the surface (in Pt<sub>1</sub>Co<sub>20</sub> and Pt<sub>1</sub>Co<sub>50</sub>), limiting the number of Pt-Co dual sites and then reducing the ORR activity. The reduction of Pt content to a large extent will sacrifice the activity due to the less number of Pt-Co active sites (in the case of Pt<sub>1</sub>Co<sub>150</sub>). This explains well the optimal activity achieved by the catalyst with the Pt: Co ratio of 1:100. Therefore, the most efficient utilization is the maximization of the surface Pt-Co dual sites while avoiding the formation of Pt-Pt bonds.

### 4. Conclusions

In summary, the synthesized SAA containing Pt-Co dual sites wrapped in nitrogen-doped graphite-carbon nanotubes delivered highly efficient ORR performance even under low Pt content. Particularly, the Pt<sub>1</sub>Co<sub>100</sub>/N-GCNT catalyst achieved an ORR mass activity of 0.81 A mg<sup>-1</sup><sub>Pt</sub> at 0.90 V (versus the RHE) outperforming Pt/C for nearly 5.4 times. Combined with the spectroscopic characterization and theoretical calculations, the excellent ORR performance to the unique Pt-Co dual sites in SAA that facilitates the immobilization of OOH\* and the dissociation of OH\* was proposed, endowing the key intermediates to adsorb and desorb smoothly over the Pt-Co dual sites, and thus circumventing the undesired 2e- ORR pathway commonly observed in most Pt SACs. Besides, the superiority of this catalyst was embodied in their excellent stability and barely faded activity even after 30,000 potential-scanning cycles, which was induced by the unique N-GCNT encapsulated stack that prevented acidic corrosion. The rational construction of such Pt-Co dual sites based SAA catalyst shed new lights on the further catalysts design on not only ORR but also beyond such as HER, OER, and also CO<sub>2</sub> electrolysis.

### CRediT authorship contribution statement

**Xing Cheng:** Conceptualization, Formal analysis, Methodology, Investigation, Writing – original draft. **Yueshuai Wang:** Data curation. **Yue Lu:** Methodology, Data curation. **Lirong Zheng:** Formal analysis, Data curation. **Shaorui Sun:** Data curation. **Hongyi Li:** Funding acquisition, Data curation. **Ge Chen:** Funding acquisition, Data curation, Writing – review & editing, Supervision. **Jiujun Zhang:** Data curation, Writing – review & editing.

### Declaration of Competing Interest

The authors declare that they have no known competing financial

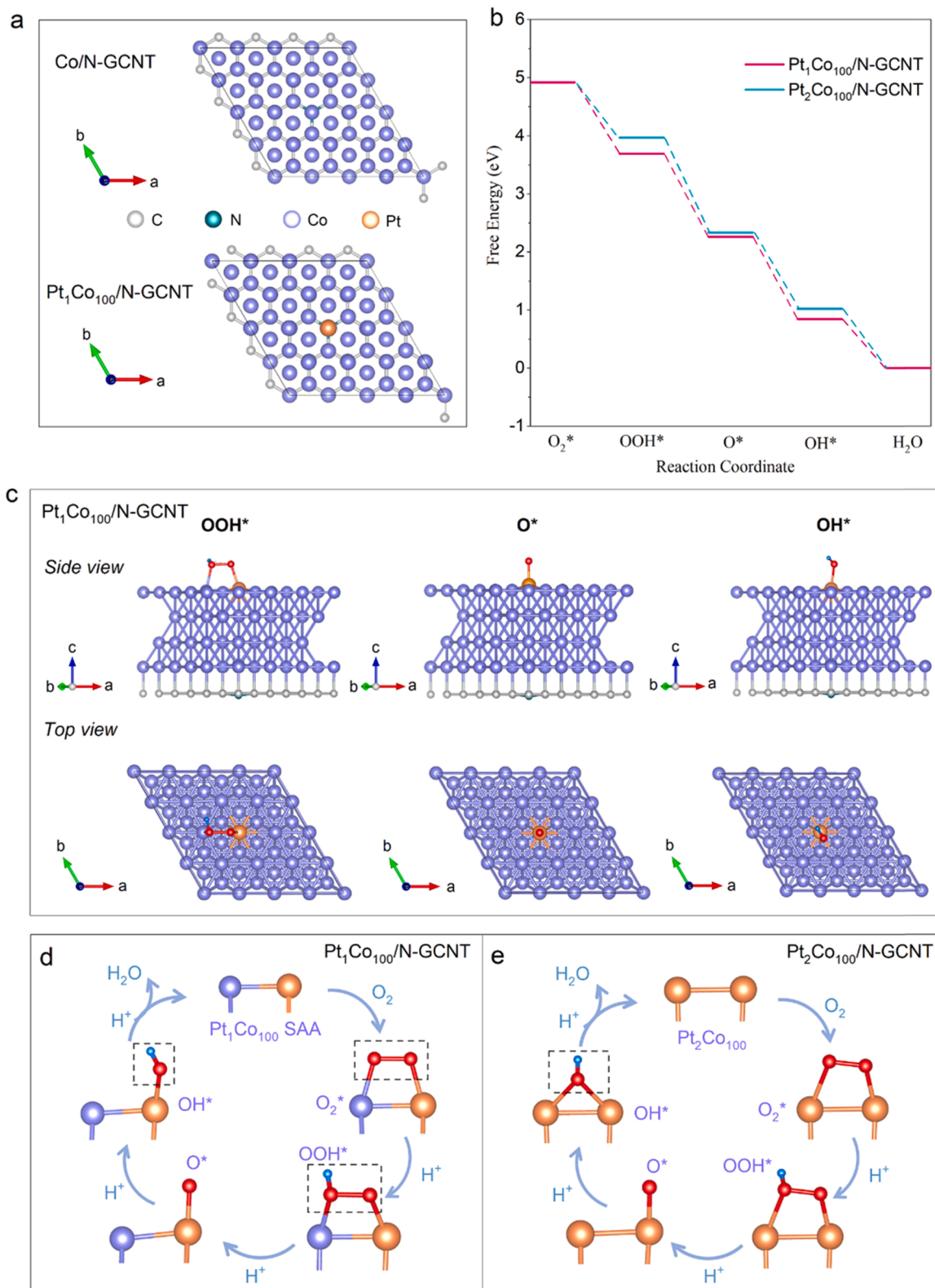


**Fig. 5.** (a) Crystal structures viewed from top sight of the Co/N-GCNT and Pt<sub>1</sub>Co<sub>100</sub>/N-GCNT catalysts after DFT optimization. (b) Calculated free-energy diagram of the ORR pathways of Pt<sub>1</sub>Co<sub>100</sub>/N-GCNT and Pt<sub>2</sub>Co<sub>100</sub>/N-GCNT ( $U = 0$ ). (c) Side and top views of the optimized structures of different intermediates on the Pt<sub>1</sub>Co<sub>100</sub>/N-GCNT catalyst. The proposed ORR mechanism of (d) Pt<sub>1</sub>Co<sub>100</sub>/N-GCNT and (e) Pt<sub>2</sub>Co<sub>100</sub>/N-GCNT. (grey, carbon; purple, cobalt; orange, platinum; red, oxygen; blue, hydrogen).

interests or personal relationships that could have appeared to influence the work reported in this paper.

## Acknowledgements

This work was supported by the National Natural Science Foundation of China (NSFC 12075015) and Beijing Municipal Great Wall Scholar Training Plan Project (CIT&TCD20190307). The authors thank the BL1W1B and 4B7B in BSRF.

## Appendix A. Supporting information

Supplementary data associated with this article can be found in the online version at doi:10.1016/j.apcatb.2022.121112.

## References

- [1] Y. He, Q. Tan, L. Lu, J. Sokolowski, G. Wu, Metal-nitrogen-carbon catalysts for oxygen reduction in PEM fuel cells: self-template synthesis approach to enhancing catalytic activity and stability, *Electrochim. Energ. Rev.* 2 (2019) 231–251.
- [2] Y. Bing, H. Liu, L. Zhang, D. Ghosh, J. Zhang, Nanostructured Pt-alloy electrocatalysts for PEM fuel cell oxygen reduction reaction, *Chem. Soc. Rev.* 39 (2010) 2184–2202.
- [3] F. Luo, A. Roy, L. Silvioli, D.A. Cullen, A. Zitolo, M.T. Sougrati, I.C. Oguz, T. Mineva, D. Teschner, S. Wagner, J. Wen, F. Dionigi, U.I. Kramm, J. Rossmieisl, F. Jaouen, P. Strasser, P-block single-metal-site tin/nitrogen-doped carbon fuel cell cathode catalyst for oxygen reduction reaction, *Nat. Mater.* 19 (2020) 1215–1223.
- [4] L. Bu, N. Zhang, S. Guo, X. Zhang, J. Li, J. Yao, T. Wu, G. Lu, J.Y. Ma, D. Su, X. Huang, Biaxially strained PtPb/Pt core/shell nanoplate boosts oxygen reduction catalysis, *Science* 354 (2016) 1410–1414.
- [5] P.-C. Sui, X. Zhu, N. Djilali, Modeling of PEM fuel cell catalyst layers: status and outlook, *Electrochim. Energ. Rev.* 2 (2019) 428–466.
- [6] L. Chong, J. Wen, J. Kubal, F.G. Sen, J. Zou, J. Greeley, M. Chan, H. Barkholtz, W. Ding, D.J. Liu, Ultralow-loading platinum-cobalt fuel cell catalysts derived from imidazolate frameworks, *Science* 362 (2018) 1276–1281.
- [7] W. Yu, M.D. Porosoff, J.G. Chen, Review of Pt-based bimetallic catalysis: from model surfaces to supported catalysts, *Chem. Rev.* 112 (2012) 5780–5817.
- [8] Z. Liu, Z. Zhao, B. Peng, X. Duan, Y. Huang, Beyond extended surfaces: understanding the oxygen reduction reaction on nanocatalysts, *J. Am. Chem. Soc.* 142 (2020) 17812–17827.
- [9] X. Wang, Z. Li, Y. Qu, T. Yuan, W. Wang, Y. Wu, Y. Li, Review of metal catalysts for oxygen reduction reaction: from nanoscale engineering to atomic design, *Chem* 5 (2019) 1486–1511.
- [10] X. Tian, X. Zhao, Y.Q. Su, L. Wang, H. Wang, D. Dang, B. Chi, H. Liu, E.J. M. Hensen, X.W.D. Lou, B.Y. Xia, Engineering bunched Pt-Ni alloy nanocages for efficient oxygen reduction in practical fuel cells, *Science* 366 (2019) 850–856.
- [11] X. Huang, Z. Zhao, L. Cao, Y. Chen, E. Zhu, Z. Lin, M. Li, A. Yan, A. Zettl, Y. M. Wang, X. Duan, T. Mueller, Y. Huang, High-performance transition metal-doped Pt<sub>3</sub>Ni octahedra for oxygen reduction reaction, *Science* 348 (2015) 1230–1234.
- [12] Q. Cheng, S. Yang, C. Fu, L. Zou, Z. Jiang, J. Zhang, H. Yang, High-loaded sub-6 nm Pt<sub>1</sub>Co<sub>1</sub> intermetallic compounds with highly efficient performance expression in PEMFCs, *Energy Environ. Sci.* (2022), <https://doi.org/10.1039/D1EE02530A>.
- [13] J. Liu, M. Jiao, L. Lu, H.M. Barkholtz, Y. Li, Y. Wang, L. Jiang, Z. Wu, D.J. Liu, L. Zhuang, C. Ma, J. Zeng, B. Zhang, D. Su, P. Song, W. Xing, W. Xu, Y. Wang, Z. Jiang, G. Sun, High performance platinum single atom electrocatalyst for oxygen reduction reaction, *Nat. Commun.* 8 (2017) 15938.
- [14] J. Liu, M. Jiao, B. Mei, Y. Tong, Y. Li, M. Ruan, P. Song, G. Sun, L. Jiang, Y. Wang, Z. Jiang, L. Gu, Z. Zhou, W. Xu, Carbon-supported divacancy-anchored platinum single-atom electrocatalysts with superhigh Pt utilization for the oxygen reduction reaction, *Angew. Chem. Int. Ed.* 58 (2019) 1163–1167.
- [15] J. Bak, J. Roh, K.-S. Lee, A. Cho, J.W. Han, E. Cho, Reconstructing the coordination environment of platinum single-atom active sites for boosting oxygen reduction reaction, *ACS Catal.* 11 (2020) 466–475.
- [16] X. Zhong, S. Ye, J. Tang, Y. Zhu, D. Wu, M. Gu, H. Pan, B. Xu, Engineering Pt and Fe dual-metal single atoms anchored on nitrogen-doped carbon with high activity and durability towards oxygen reduction reaction for zinc-air battery, *Appl. Catal. B* 286 (2021), 119891.
- [17] S. Li, J. Liu, Z. Yin, P. Ren, L. Lin, Y. Gong, C. Yang, X. Zheng, R. Cao, S. Yao, Y. Deng, X. Liu, L. Gu, W. Zhou, J. Zhu, X. Wen, B. Xu, D. Ma, Impact of the coordination environment on atomically dispersed Pt catalysts for oxygen reduction reaction, *ACS Catal.* 10 (2019) 907–913.
- [18] R. Gao, J. Wang, Z.-F. Huang, R. Zhang, W. Wang, L. Pan, J. Zhang, W. Zhu, X. Zhang, C. Shi, J. Lim, J.-J. Zou, Pt/Fe<sub>2</sub>O<sub>3</sub> with Pt-Fe pair sites as a catalyst for oxygen reduction with ultralow Pt loading, *Nat. Energy* 6 (2021) 614–623.
- [19] Y. Chen, R. Gao, S. Ji, H. Li, K. Tang, P. Jiang, H. Hu, Z. Zhang, H. Hao, Q. Qu, X. Liang, W. Chen, J. Dong, D. Wang, Y. Li, Atomic-level modulation of electronic density at cobalt single-atom sites derived from metal-organic frameworks: enhanced oxygen reduction performance, *Angew. Chem. Int. Ed.* 60 (2021) 3212–3221.
- [20] A. Han, X. Wang, K. Tang, Z. Zhang, C. Ye, K. Kong, H. Hu, L. Zheng, P. Jiang, C. Zhao, Q. Zhang, D. Wang, Y. Li, An adjacent atomic platinum site enables single-atom iron with high oxygen reduction reaction performance, *Angew. Chem. Int. Ed.* 60 (2021) 19262–19271.
- [21] S. Yang, J. Kim, Y.J. Tak, A. Soon, H. Lee, Single-atom catalyst of platinum supported on titanium nitride for selective electrochemical reactions, *Angew. Chem. Int. Ed.* 55 (2016) 2058–2062.
- [22] N. Cheng, L. Zhang, K. Doyle-Davis, X. Sun, Single-atom catalysts: from design to application, *Electrochim. Energ. Rev.* 2 (2019) 539–573.
- [23] C.H. Choi, M. Kim, H.C. Kwon, S.J. Cho, S. Yun, H.T. Kim, K.J. Mayrhofer, H. Kim, M. Choi, Tuning selectivity of electrochemical reactions by atomically dispersed platinum catalyst, *Nat. Commun.* 7 (2016) 10922.
- [24] R. Shen, W. Chen, Q. Peng, S. Lu, L. Zheng, X. Cao, Y. Wang, W. Zhu, J. Zhang, Z. Zhuang, C. Chen, D. Wang, Y. Li, High-concentration single atomic Pt sites on hollow Cu<sub>x</sub> for selective O<sub>2</sub> reduction to H<sub>2</sub>O<sub>2</sub> in acid solution, *Chem* 5 (2019) 2099–2110.
- [25] S. Yang, Y.J. Tak, J. Kim, A. Soon, H. Lee, Support effects in single-atom platinum catalysts for electrochemical oxygen reduction, *ACS Catal.* 7 (2017) 1301–1307.
- [26] H.E. Kim, I.H. Lee, J. Cho, S. Shin, H.C. Ham, J.Y. Kim, H. Lee, Palladium single-atom catalysts supported on C@C<sub>3</sub>N<sub>4</sub> for electrochemical reactions, *Chem. Electro. Chem.* 6 (2019) 4757–4764.
- [27] S. Liu, S. Huang, Theoretical insights into the activation of O<sub>2</sub> by Pt single atom and Pt<sub>4</sub> nanocluster on functionalized graphene support: Critical role of Pt positive polarized charges, *Carbon* 115 (2017) 11–17.
- [28] R.T. Hannagan, G. Giannakakis, M. Flytzani-Stephanopoulos, E.C.H. Sykes, Single-atom alloy catalysis, *Chem. Rev.* 120 (2020) 12044–12088.
- [29] T. Zhang, A.G. Walsh, J. Yu, P. Zhang, Single-atom alloy catalysts: structural analysis, electronic properties and catalytic activities, *Chem. Soc. Rev.* 50 (2021) 569–588.
- [30] J. Jiao, R. Lin, S. Liu, W.C. Cheong, C. Zhang, Z. Chen, Y. Pan, J. Tang, K. Wu, S. F. Hung, H.M. Chen, L. Zheng, Q. Lu, X. Yang, B. Xu, H. Xiao, J. Li, D. Wang, Q. Peng, C. Chen, Y. Li, Copper atom-pair catalyst anchored on alloy nanowires for selective and efficient electrochemical reduction of CO<sub>2</sub>, *Nat. Chem.* 11 (2019) 222–228.
- [31] C.H. Chen, D. Wu, Z. Li, R. Zhang, C.G. Kuai, X.R. Zhao, C.K. Dong, S.Z. Qiao, H. Liu, X.W. Du, Ruthenium-based single-atom alloy with high electrocatalytic activity for hydrogen evolution, *Adv. Energy Mater.* 9 (2019), 1803913.
- [32] J. Lee, A. Kumar, T. Yang, X. Liu, A.R. Jadhav, G.H. Park, Y. Hwang, J. Yu, C.T. K. Nguyen, Y. Liu, S. Ajmal, M.G. Kim, H. Lee, Stabilizing the OOH<sup>\*</sup> intermediate via pre-adsorbed surface oxygen of a single Ru atom-bimetallic alloy for ultralow overpotential oxygen generation, *Energy Environ. Sci.* 13 (2020) 5152–5164.
- [33] R.T. Hannagan, G. Giannakakis, R. Réocreux, J. Schumann, J. Finzel, Y. Wang, A. Michaelides, P. Deshlahra, P. Christopher, M. Flytzani-Stephanopoulos, M. Stamatakis, E.C.H. Sykes, First-principles design of a single-atom–alloy propane dehydrogenation catalyst, *Science* 372 (2021) 1444–1447.
- [34] X.X. Wang, S. Hwang, Y.T. Pan, K. Chen, Y. He, S. Karakalos, H. Zhang, J. S. Spendelow, D. Su, G. Wu, Ordered Pt<sub>3</sub>Co intermetallic nanoparticles derived from metal-organic frameworks for oxygen reduction, *Nano Lett.* 18 (2018) 4163–4171.
- [35] D. Wang, H.L. Xin, R. Hovden, H. Wang, Y. Yu, D.A. Muller, F.J. DiSalvo, H. D. Abruna, Structurally ordered intermetallic platinum-cobalt core-shell nanoparticles with enhanced activity and stability as oxygen reduction electrocatalysts, *Nat. Mater.* 127 (2013) 81–88.
- [36] D.S. Choi, A.W. Robertson, J.H. Warner, S.O. Kim, H. Kim, Low-temperature chemical vapor deposition synthesis of Pt-Co alloyed nanoparticles with enhanced oxygen reduction reaction catalysis, *Adv. Mater.* 28 (2016) 7115–7122.
- [37] M. Newville, IFEFFIT: interactive XAFS analysis and FEFF fitting, *J. Synchrotron Radiat.* 8 (2001) 322–324.
- [38] G. Kresse, J. Furthmüller, Efficiency of ab-initio total energy calculations for metals and semiconductors using a plane-wave basis set, *Comp. Mater. Sci.* 6 (1996) 15–50.
- [39] P.E. Blöchl, Projector augmented-wave method, *Phys. Rev. B* 50 (1994) 17953–17979.
- [40] J.P. Perdew, J.A. Chevary, S.H. Vosko, K.A. Jackson, M.R. Pederson, D.J. Singh, C. Fiolhais, Erratum: atoms, molecules, solids, and surfaces: applications of the generalized gradient approximation for exchange and correlation, *Phys. Rev. B* 48 (1993) 4978.
- [41] S. Grimme, J. Antony, S. Ehrlich, H. Krieg, A consistent and accurate ab initio parametrization of density functional dispersion correction (DFT-D) for the 94 elements H–Pu, *Chem. Phys.* 132 (2010), 154104.
- [42] J. Rossmeisl, A. Logadottir, J.K. Nørskov, Electrolysis of water on (oxidized) metal surfaces, *Chem. Phys.* 319 (2005) 178–184.
- [43] X. Cheng, Y. Lu, L. Zheng, Y. Cui, M. Niibe, T. Tokushima, H. Li, Y. Zhang, G. Chen, S. Sun, J. Zhang, Charge redistribution within platinum-nitrogen coordination structure to boost hydrogen evolution, *Nano Energy* 73 (2020), 104739.
- [44] X. Shen, X. Liu, S. Wang, T. Chen, W. Zhang, L. Cao, T. Ding, Y. Lin, D. Liu, L. Wang, W. Zhang, T. Yao, Synergistic modulation at atomically dispersed Fe/Au interface for selective CO<sub>2</sub> electroreduction, *Nano Lett.* 21 (2021) 686–692.
- [45] J. Deng, L. Yu, D. Deng, X. Chen, F. Yang, X. Bao, Highly active reduction of oxygen on a FeCo alloy catalyst encapsulated in pod-like carbon nanotubes with fewer walls, *J. Mater. Chem. A* 1 (2013) 14868–14873.
- [46] L. An, N. Jiang, B. Li, S. Hua, Y. Fu, J. Liu, W. Hao, D. Xia, Z. Sun, A highly active and durable iron/cobalt alloy catalyst encapsulated in N-doped graphitic carbon nanotubes for oxygen reduction reaction catalyzed by a nanofibrous dicyandiamide template, *J. Mater. Chem. A* 6 (2018) 5962–5970.

[47] L. Guo, W.-J. Jiang, Y. Zhang, J.-S. Hu, Z.-D. Wei, L.-J. Wan, Embedding Pt nanocrystals in N-doped porous carbon/carbon nanotubes toward highly stable electrocatalysts for the oxygen reduction reaction, *ACS Catal.* 5 (2015) 2903–2909.

[48] C. Zhao, Y. Wang, Z. Li, W. Chen, Q. Xu, D. He, D. Xi, Q. Zhang, T. Yuan, Y. Qu, J. Yang, F. Zhou, Z. Yang, X. Wang, J. Wang, J. Luo, Y. Li, H. Duan, Y. Wu, Y. Li, Solid-diffusion synthesis of single-atom catalysts directly from bulk metal for efficient CO<sub>2</sub> reduction, *Joule* 3 (2019) 584–594.

[49] M.X. Chen, L. Tong, H.W. Liang, Understanding the catalytic sites of metal-nitrogen-carbon oxygen reduction electrocatalysts, *Chem. Eur. J.* 27 (2021) 145–157.

[50] U.I. Kramm, I. Herrmann-Geppert, J. Behrends, K. Lips, S. Fiechter, P. Bogdanoff, On an easy way to prepare metal-nitrogen doped carbon with exclusive presence of MeN<sub>4</sub>-type sites active for the ORR, *J. Am. Chem. Soc.* 138 (2016) 635–640.